Desalination and Water Treatment
www.deswater.com
doi: 10.5004/dwt.2020.25938

196 (2020) 177–188
August

Synthesis and characterization of heterogeneous catalyst EDTMPA-Cu-LDH and study of the mechanism of visible-light photocatalytic degradation of Rhodamine B

Huali Zhang[a], Jiaxin Zhang[a], Hanjun Wu[a,*], Yi Pan[a], Yan Xia[a], Zhiquan Pan[a], Dongshen Wang[b]

[a]*School of Chemistry and Environmental Engineering, Wuhan Institute of Technology, Wuhan 430074, Hubei, China, Tel. +(86) 13419543795; emails: wuhj1204@126.com (H.J. Wu), zhanghl413@126.com (H.L. Zhang), 15107104732@163.com (J.X. Zhang), 332373976@qq.com (Y. Pan), 921004152@qq.com (Y. Xia), zhiqpan@163.com (Z.Q. Pan)*
[b]*State Key Laboratory of Environmental Aquatic Chemistry, Research Center for Eco-Environmental Sciences, Chinese Academy of Sciences, Beijing 100085, China, email: wgds@rcees.ac.cn (D.S. Wang)*

Received 18 November 2019; Accepted 3 April 2020

ABSTRACT

In this work, heterogeneous catalysts of Cu(II)-ethylenediamine tetramethylene phosphonic acid (Cu(II)-EDTMPA) complex intercalated layered double hydroxides (EDTMPA-Cu-LDH) was synthesized by co-precipitation method for visible-light photocatalytic degradation of Rhodamine B (RhB). The synthesized catalysts were characterized by X-ray diffraction, Fourier-transform infrared spectroscopy, scanning electron microscopy, transmission electron microscopy, UV-Vis diffuse reflectance spectroscopy, and X-ray photoelectron spectroscopy. The results indicated that the EDTMPA-Cu-LDH showed a typical layered structure. After intercalation, layer spacing increased from 7.96 to 12.21 Å. The catalysts showed excellent catalytic activity for the degradation of RhB in visible light. The optimum conditions for RhB degradation were confirmed to be natural initial pH value 5.85, 10 mmol L^{-1} of RhB concentration, 7 mmol L^{-1} of H_2O_2 concentration, and 0.3 g L^{-1} of catalyst dosage. The maximum degradation efficiency was 98.2% under the optimum conditions and excellent reusability and stability were obtained in the regeneration test. In the end, the reaction mechanism that might exist in the heterogeneous UV-Fenton system was proposed.

Keywords: Heterogeneous catalyst; Rhodamine B; Photocatalysis; Cu(II)-ethylenediamine tetramethylene phosphonic acid-LDH

1. Introduction

Nowadays, with the replacement of new products and technologies, the demand for synthetic chemicals in many industries is increasing. As a large industrial country, China's industrial wastewater volume is increasing, of which dyes account for a large proportion [1]. Dyes come from textile, printing, and photographic industries. And more than 1.6×10^9 m^3 of dye-containing wastewater per year drains into the environmental water system without treatment [2], leading to severe damage to human health and water environment [3]. Rhodamine B (RhB) occupied a large proportion of the printing and dyeing industry because of its strong coloring power. Due to imperfect cleaning and processing technology, the printing and dyeing industry had caused a large number of dyes to be discharged from the waste liquid. The complex components and high color are the characteristics of this type of dye waste liquid. RhB,

* Corresponding author.

as a triphenylmethane dye, used triphenylmethane as its parent. Its molecular structure was a unique structure with three benzene rings attached to the central carbon atom, which made it difficult to be degraded in the environment. RhB dye had certain toxicity, which could produce carcinogenic, teratogenic, and mutagenic effects on mammalian cells and high chroma would affect the photosynthesis of plants in water [4–6]. Therefore, it is particularly important to find a method for treating wastewater efficiently.

In recent years, a considerable amount of research has been carried out on the removal of organic pollutants, such as adsorption, photocatalytic, and biodegradation [7]. Among these methods, advanced oxidation processes (AOPs), including homogeneous and heterogeneous Fenton, ozonation, and photo-Fenton processes, are considered to be the most promising method for treating contaminated wastewater because of its strong oxidation ability and no secondary pollution [8]. The hydroxyl radical (•HO) is generated to improve the degradation efficiency during the oxidation processes of AOPs [9]. Among the AOPs, Fenton technology has the characteristics of high processing efficiency, low-cost, and easy industrialization, and has gradually become one of the main methods in AOPs [10,11]. However, for the homogeneous Fenton system, it can only be carried out effectively at a lower pH [12]. And because the catalyst of the homogenous Fenton system is mixed in the wastewater, a large amount of iron-containing sludge will be produced after the reaction, causing secondary pollution. In order to solve these problems, the research of heterogeneous catalysts has gained great attention. Heterogeneous Fenton technology uses solid-phase catalysts, achieving catalysts recovery, and recycling. Furthermore, catalytic reactions can be carried out in a wide pH range [13]. Palanivel [14] reported a novel heterostructure ($ZnFe_2O_4$/g-C_3N_4) nanocomposite. The composite catalyst showed the enhanced photocatalytic activity and high electrochemical specific capacitance of 103 F/g at 10 A/g of current density. The 95% of degradation efficiency was maintained after 5 cycles of photocatalytic activity and 94% of capacitance retaining at a current density of 10 A/g after 500 cycles. Xian [15] prepared the carbon quantum dot (CQD)-decorated $BiFeO_3$ nanoparticle photocatalysts. CQD/$BiFeO_3$ composites exhibited significantly improved photocatalytic and photo-Fenton catalytic activities. The 12C/$BiFeO_3$ composite displayed the optimal degradation percentage of ~73% after 3 h irradiation, which was 2.2 times higher than that of bare $BiFeO_3$. And about 96% of AO7 was photo-Fenton catalytically degraded over 12C/BFO sample under 3 h irradiation.

Copper-containing catalysts have been extensively studied for their high activity and low price, and are used as catalysts for heterogeneous Fenton reactions [16]. Copper-based materials have similar redox properties to iron and the copper-based Fenton system has a higher operating range than the iron-based Fenton system. More importantly, Cu^{2+} is more likely to be reduced by hydrogen peroxide (H_2O_2) than Fe^{3+} and the Cu^{2+}-H_2O_2 Fenton system has a higher reaction rate than the Fe^{2+}-H_2O_2 system. It can produce •OH more efficiently [17]. Singh [18] prepared copper oxide (CuO) nanoneedles by the spotlight. CuO nanoneedles demonstrated brilliant degradation capacity of cationic (VB) and anionic (DR) dye in the existence of UV-visible radiations. Kayalvizhi [19] explored the eco-friendly green synthesis of CuONPs using *Annona muricata* leaf extract. CuONPs exhibited highly degradation capacity of Reactive Red 120 (RR120) and Methyl Orange (MO) under sunlight irradiation, which was 90% and 95% decolorization efficiency at 60 min, respectively.

The possible catalytic mechanism is that Cu^{2+} is first reduced by H_2O_2 to Cu^+ [Eq. (1)], and then further reacted with H_2O_2 to form high reactive oxygen species HO• [Eq. (2)] [20].

$$Cu^{2+} + H_2O_2 \rightarrow Cu^+ + HO_2^{\bullet} + OH^- \quad (1)$$

$$Cu^+ + H_2O_2 \rightarrow Cu^{2+} + HO^{\bullet} + HO^- \quad (2)$$

Layered double hydroxides (LDHs) provide a stable solvent entity by embedding transition metal complexes by intercalation method due to its special layered structure.

The typical LDH compound is the naturally occurring mineral hydrotalcite, which has the formula $Mg_6Al_2(OH)_{16}CO_3{\cdot}4H_2O$. LDHs have the general formula $[M^{II}_{1-x}M^{III}_x(OH)_2]^{x+}[A_{x/n}{\cdot}H_2O]_x$, where $M^{II} = Mg^{2+}$, Fe^{2+}, Co^{2+}, Zn^{2+}, etc. $M^{III} = Al^{3+}$, Fe^{3+}, Cr^{3+}, etc. and A^{n-} is the interlayer anion [21,22]. Due to their many characteristics such as layer cation ion son-in-control, inter-layer anion exchangeable, thermal stability, and memory function. LDHs have been extensively studied for many applications [23,24]. Dorraji et al. [25] synthesized the ZnS/ZnNiAl-LDH/GO nanocomposite via co-precipitation method. The maximum decolorization efficiency of Reactive Red 43 was 86% when ZnS/ZnNiAl-LDH/GO nanocomposite was used. Nayak et al. [26] designed a novel heterostructure MoS_2/NiFe LDH. The as-synthesized MSLDH3 showed superior photocatalytic activities in the degradation of RhB with H_2 evolution and recyclability.

This work aims to synthesize a kind of new heterogeneous photo-Fenton catalyst which can be recovered easily and degrade dyes efficiently under the visible light region. Ethylenediamine tetramethylene phosphonic acid complex intercalated layered double hydroxides (EDTMPA-Cu-LDH) was prepared by the co-precipitation method and acted as a heterogeneous catalyst can almost completely degrade RhB within 120 min. The reusability and photocatalytic degradation mechanism of EDTMPA-Cu-LDH was also assessed. The novel heterogeneous photo-Fenton catalysts are expected to be applicable in water treatment contaminated by organic matters.

2. Materials and methods

2.1. Materials

All chemicals magnesium nitrate hexahydrate ($Mg(NO_3)_2{\cdot}6H_2O$), aluminum nitrate nonahydrate ($Al(NO_3)_3{\cdot}9H_2O$), copper nitrate trihydrate ($Cu(NO_3)_2{\cdot}3H_2O$), RhB, hydrogen peroxide (H_2O_2) were purchased from Sinopharm Chemical Reagent Co. Ltd. Ethylenediamine tetramethylenephosphonic acid ($C_6H_{20}N_2O_{12}P_4$; EDTMPA) was obtained from Aladdin Reagent Co. Ltd. Hydrochloric acid and sodium hydroxide (NaOH) was obtained from Fuchen Chemical Reagent Co. Ltd. All chemicals were analytical grade with

no more purification before use. Ultrapure water, from which CO_2 was removed, was used throughout the experiment.

2.2. Synthesis of EDTMPA-Cu-LDH

2.2.1. Preparation of MgAl-NO_3-LDH

The MgAl-LDH was synthesized by the co-precipitation method. $Mg(NO_3)_2{\cdot}6H_2O$ (0.06 mol) and $Al(NO_3)_3{\cdot}9H_2O$ (0.02 mol) were dissolved in 200 mL ultrapure water. The pH value of the above-mixed solution was controlled at about 9 by the addition of dilute sodium hydroxide solutions with a concentration of 0.4 mol L^{-1}. The resulting suspension was aged at 90°C for 24 h. Finally, the precipitation was filtered and washed until the supernatant became neutral with ultrapure water, then dried at 50°C for 30 h.

2.2.2. Preparation of EDTMPA-Cu(II) complex

EDTMPA (5 mmol) was dissolved in 25 ml solution of NaOH (10 mmol), which was donated as solution A. $Cu(NO_3)_2{\cdot}3H_2O$ (15 mmol) was dissolved in 20 ml ultrapure water, which was donated as solution B. Immediately, solution B was added to solution A, stirring for 12 h at room temperature.

2.2.3. Preparation of EDTMPA-Cu-LDH

2 g sample of the synthesized MgAl-LDH was dissolved in 100 ml ultrapure water, stirring for 24 h at room temperature, which was donated as solution C. Then solution C has dispersed into the EDTMPA-Cu(II)-anion exchange solution, stirring for 12 h at room temperature. The precipitation was filtered and washed until the supernatant became neutral with ultrapure water, then dried at 50°C for 30 h. The final products were denoted as EDTMPA-Cu-LDH.

2.3. Materials characterization

Infrared spectra were recorded in Fourier-transform infrared spectroscopy (FT-IR) Nicolet iS50 spectrometer (Nicolet, America) in the 4,000–400 cm^{-1} range using powdered samples diluted in KBr pellets. X-ray diffraction (XRD) patterns were recorded with an X'Pert Pro (PANalytical, Holland) diffractometer (using Cu KR radiation with a scan speed of 2° (2θ) min^{-1}. Scanning electron microscopy (SEM) was carried out with SU 8010 (Hitachi, Japan). Transmission electron microscopy (TEM) was carried out with JEM 2100F (JEOL, Japan). X-ray photoelectron spectroscopy (XPS) was measured on Thermo ESCALAB 250XI (Thermo Fisher Scientific, America). UV-Vis diffuse reflectance spectroscopy (UV-Vis DRS) of the powdered samples were recorded in a PE lambda 750S (PerkinElmer, America) spectrophotometer.

2.4. Photocatalytic reaction

The standard curve for the RhB was prepared by measuring the absorbance values for a series of known concentrations of RhB solutions at the wavelength of maximum absorbance (λ = 554 nm). The photo-Fenton experiments were performed in a batch reactor using artificial visible light produced by a 500 W xenon lamp. To start with, the catalyst was added to a magnetically stirred RhB solution and stirred under dark conditions for 30 min to achieve adsorption equilibrium. Then, H_2O_2 was added, and during irradiation, 4 ml of the sample solution was taken out at pre-set time intervals, centrifuged, and the absorbance of the upper layer liquid was measured using a UV-visible spectrophotometer. The photodegradation reaction was studied by changing the parameters. Particularly, the pH range RhB solution was adjusted between 3 and 9; the initial RhB dye concentration was between 10 and 70 mmol L^{-1}; the H_2O_2 concentration was between 1 and 10 mmol L^{-1} and the catalyst dosage was between 0.1 and 0.5 g L^{-1}. The desired value pH of the dye solution was obtained by adding 0.1 mol L^{-1} HCl or 0.1 mol L^{-1} NaOH aqueous solution. The active species produced in the photo-degradation reactions were tested by using different scavengers such as $NaHCO_3$, isopropanol, chloroform, and potassium bromate for scavenging hole (h^+), hydroxyl radical ($^{\bullet}OH$), superoxide radicals ($^{\bullet}O_2^-$) and electron (e^-), respectively. The scavenger tests were carried out at optimum conditions, where the degradation efficiency was maximum.

The photodegradation kinetics was evaluated under each parameter on the RhB degradation experiment, which was aimed at understanding the reaction characteristics of the RhB dye under visible light. The plot of $\ln(C_0/C_t)$ vs. irradiation time was close to linearity, which indicated that RhB degradation followed by a first-order kinetic model represented by Eq. (3).

$$-\ln\left(\frac{C_0}{C_t}\right) = k \cdot t \tag{3}$$

where C_0 is the initial concentration of the dye and C_t is the concentration at time t and k is the kinetic rate constant. The value of k was obtained from the slope and the intercept of the linear plot.

3. Results and discussion

3.1. Characterization of MgAl-LDH and EDTMPA-Cu-LDH

3.1.1. XRD analysis

The XRD patterns of MgAl-LDH and EDTMPA-Cu-LDH composites are presented in Fig. 1. LDHs at (003), (006), (009), (110), and (113) indicated the typical hydrotalcite structure [27]. The diffraction peaks of the (003), (006), and (009) crystal faces appeared at 11.1°, 22.43°, and 34.42° respectively, which were basically consistent with the diffraction peak angles of the crystal faces of the MgAl-NO_3-LDH XRD spectrum [28,29]. The diffraction peaks of EDTMPA-Cu-LDH at (003), (006), (009) crystal faces were obviously shifted to low angles. And the characteristic peaks of EDTMPA-Cu-LDH appeared when 2θ was 7.24° (003), 11.306° (006), 19.87° (009). The basal spacing (d_{003}) of the MgAl-LDH and EDTMPA-Cu-LDH were 7.96 and 12.21 Å, respectively, which was calculated by Bragg's law ($2d\sin\theta = n\lambda$) [30]. The change in d_{003} further proved that EDTMPA-Cu anions might be intercalated into the MgAl-LDH interlayer.

3.1.2. FT-IR analysis

The FT-IR spectrum of MgAl-LDH, EDTMPA, and EDTMPA-Cu-LDH composites are presented in Fig. 2. In the FT-IR spectra of MgAl-LDH and EDTMPA-Cu-LDH, the strong absorption peak at 3,480 and 1,638 cm^{-1} were attributed to the O–H band [31]. The strong characteristic peak of NO_3^- in LDH was also observed at 1,350 cm^{-1} [32]. In the FT-IR spectra of EDTMPA and EDTMPA-Cu-LDH, characteristic band at 763 cm^{-1} was ascribed to C–P stretching vibrations [33]. From the FT-IR spectrum of neat EDTMPA, a strong P–O band at 950 cm^{-1} was observed [34]. However, the P–O band was shifted to 1,070 cm^{-1} from the spectra of EDTMPA-Cu-LDH, which was due to the ionic interaction of EDTMPA with copper. The absorbance peak at 1,436 cm^{-1} was due to the vibration of the C–N band. The band at 1,193 cm^{-1} was caused by the stretching vibration of P=O [35]. But, the P=O signal had disappeared from the spectra of EDTMPA-Cu-LDH. The shifting and disappearing of the stretching vibration peaks proved that the EDTMPA-Cu anions might be intercalated into the MgAl-LDH interlayer.

3.1.3. Morphology analysis

The morphology of the composites was acquired by SEM and TEM. From Fig. 3a, it could be seen that the MgAl-LDH showed a typical lamellar structure, and particle size was uniform. The image of MgAl-LDH presented a smooth surface. Although there were overlapping phenomena between the sheets, the overall morphology was better. From Fig. 3b, the EDTMPA-Cu-LDH showed a regular flaky particle with obvious edges and corners and there were some ungrown particles. Overall, it presented a high degree of crystallizing. The TEM images of MgAl-LDH and EDTMPA-Cu-LDH were

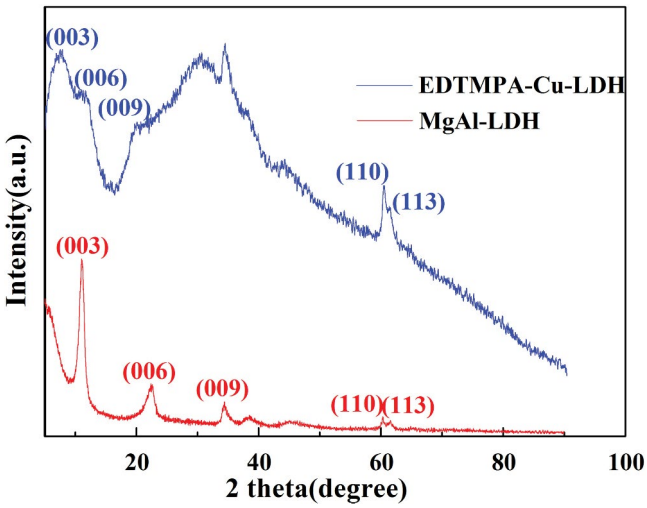

Fig. 1. XRD patterns of EDTMPA-Cu-LDH and MgAl-LDH.

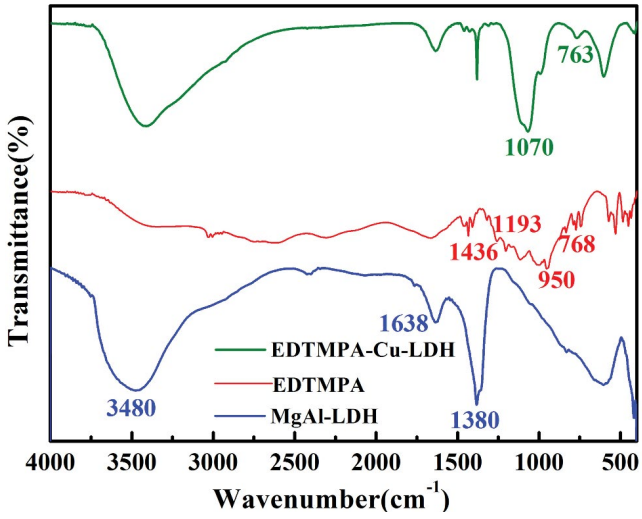

Fig. 2. FT-IR spectra of EDTMPA-Cu-LDH, EDTMPA, and MgAl-LDH.

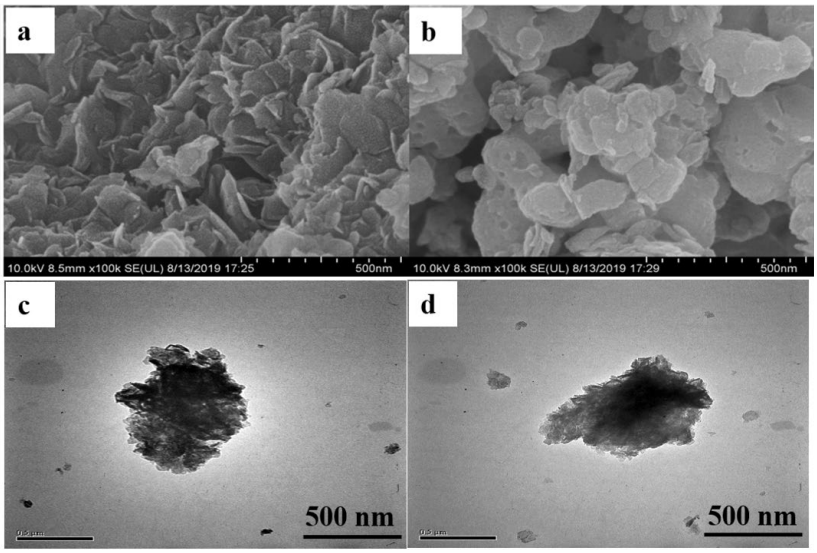

Fig. 3. SEM images of (a) MgAl-LDH, (b) EDTMPA-Cu-LDH, TEM images of (c) MgAl-LDH, and (d) EDTMPA-Cu-LDH.

shown in Figs. 3c and d. It could be seen that MgAl-LDH and EDTMPA-Cu-LDH showed characteristic hexagonal plate-like shape. The edge of the EDTMPA-Cu-LDH sheet structure was smooth and had scattered nanosheets around it. The particle size varied from 1 to 20 nm, which was consistent with the results of XRD.

3.1.4. UV-Vis DRS analysis

UV-Vis DRS and bandgap energy values of MgAl-LDH and EDTMPA-Cu-LDH are shown in Figs. 4a and b, respectively. The sample showed absorption from the UV to the visible area and the absorption edge gradually moved toward the visible range. It could be observed that MgAl-LDH had two strong UV absorptions at 202 and 302 nm, which was attributed to the existence of nitrate anions in the interlayer galleries [36]. The MgAl-LDH, whose mainly absorption band at 200–400 nm, showed weak visible light absorption. Compared to MgAl-LDH, the EDTMPA-Cu-LDH had a strong absorption band of 200–400 nm, and the absorption band of 480–800 nm was greatly enhanced. Thus, the absorption in the visible light was greatly enhanced after EDTMPA-Cu intercalation to the LDH layer.

The bandgap energy values of samples were estimated by the Kubelka–Munk (K–M) function (Eq. (4)) [37].

$$F(R)=\frac{(1-R)^2}{2R}=k/s \tag{4}$$

where $F(R)$ and R are the absolute and relative reflectance, respectively; k is the molar absorption coefficient, and s is the scattering coefficient. The bandgap of the MgAl-LDH and EDTMPA-Cu-LDH was calculated to be about 3.50 and 2.8 eV by Tauc plot through K–M function, respectively. And lower E_g value of the sample contributed to improving light absorption and photocatalytic efficiency [38]. Thus, EDTMPA-Cu-LDH could show more activity in the visible region and be used to degrade the dye under visible light.

The valence band (E_v) was also used to evaluated photocatalysis and the result is shown in Fig. 5. The E_v of EDTMPA-Cu-LDH located at 1.1 eV. Thus, the conduction band (CB) was about –1.7 eV through $E_v - E_g$.

3.1.5. XPS analysis

The chemical state of the compositional elements in EDTMPA-Cu-LDH was revealed by XPS and a representative spectrum of EDTMPA-Cu-LDH was shown in Fig. 6. The XPS spectrum for Mg 2p, Al 2p, Cu 2p, P 2p, N 1s, and O 1s are shown in Figs. 6a–6f, respectively. The XPS peak located at 49.75 eV assigned to the Mg 2p was be found in the spectrum of EDTMPA-Cu-LDH suggesting the existence of the Mg(II) species [39,40]. Two different peaks could be observed on the XPS spectrum for Al 2p, which represented two different oxygen species. The peak located at 74.4 eV was identified with the existence of Al oxide [41]. And another peak located at 76.8 eV corresponded to Al(III) [42]. The XPS peaks of $2p_{3/2}$ (932.6 eV) and $2p_{1/2}$ (952.6 eV), and their shake-up satellite peaks at 943.6 and 962.8 eV, corresponding to Cu(II), were observed [43]. From the XPS spectrum for P 2p, a single peak at 132.8 eV corresponded to P–O [44]. In the XPS spectrum for N 1s of the EDTMPA-Cu-LDH, there were two peaks at 399.7 and 406 eV. One peak

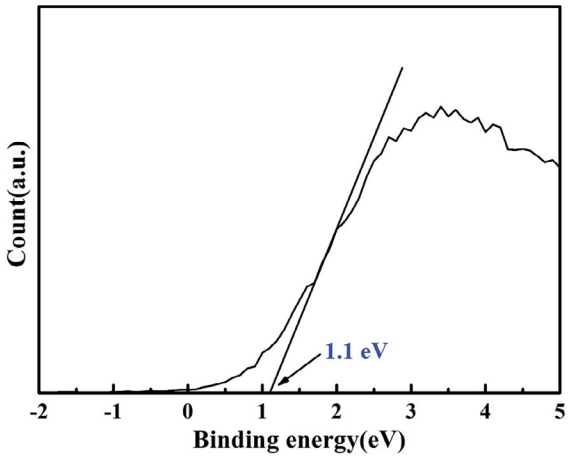

Fig. 5. The valence band XPS pattern of EDTMPA-Cu-LDH.

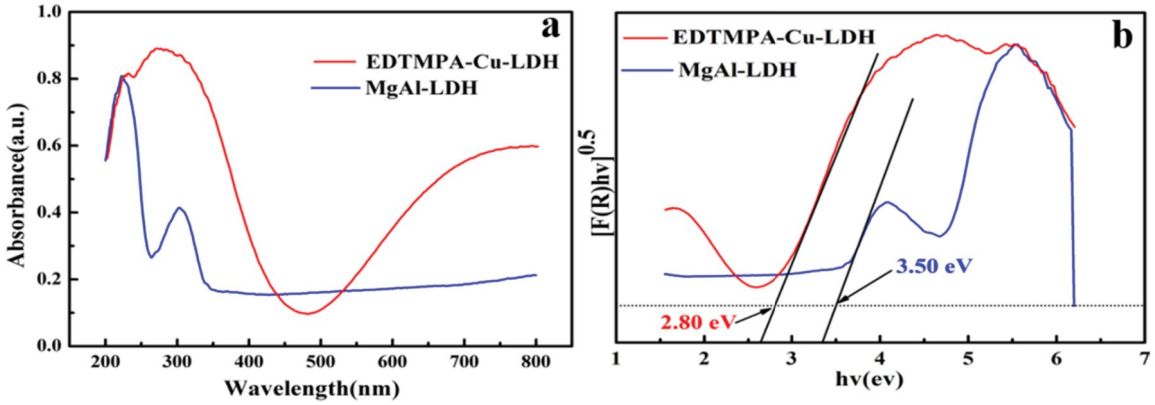

Fig. 4. (a) UV-Vis diffuse reflectance spectroscopy of EDTMPA-Cu-LDH and MgAl-LDH and (b) band gap energy values of EDTMPA-Cu-LDH and MgAl-LDH.

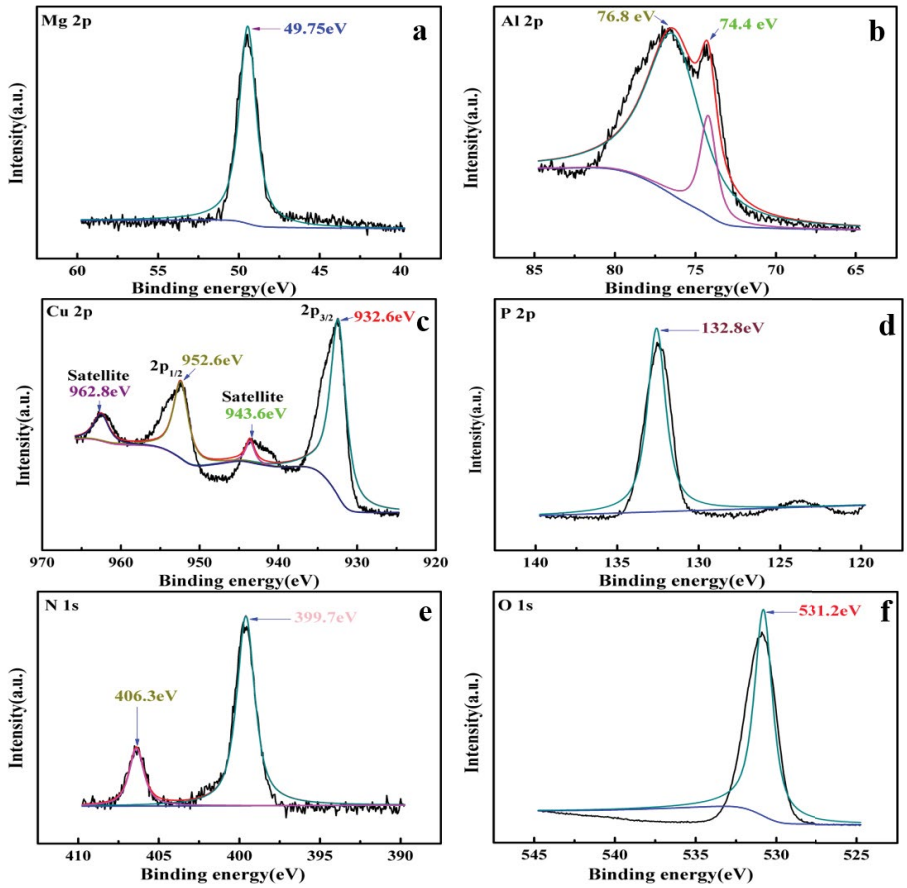

Fig. 6. (a) XPS survey for Mg 2p, (b) XPS survey for Al 2p, (c) XPS survey for Cu 2p, (d) XPS survey for P 2p, (e) XPS survey for N 1s, and (f) XPS survey for O 1s.

at 399.7 eV corresponded to C–N [45]. Another at 406 eV assigned to the NH_3^+ [46]. The O 1s spectrum showed one single peak at 531.2 eV, which corresponded to O-metal [47].

3.2. Influence of reaction parameters on catalytic activity

Experiments were carried out to investigate the influence of several parameters including solution pH, initial dye concentration, H_2O_2 concentration, and catalyst dosage on the degradation efficiency of RhB. Comparative experiments were conducted to investigate the effect of catalyst activity under light and dark conditions.

3.2.1. Evaluation of catalyst activity under light and dark conditions

The degradation efficiency of RhB was shown in Fig. 7. Four experiments were carried out to explore the degradation efficiency of RhB under light conditions. It could be clearly observed that the degradation efficiency of RhB within 120 min was only 7.38% without any additives. When adding H_2O_2, the degradation efficiency of RhB was improved to about 20.67%. In addition, the degradation efficiency of RhB was only 6.89%, when the only catalyst was added. When both catalyst and H_2O_2 were added to the dye solution, the degradation efficiency of RhB was greatly

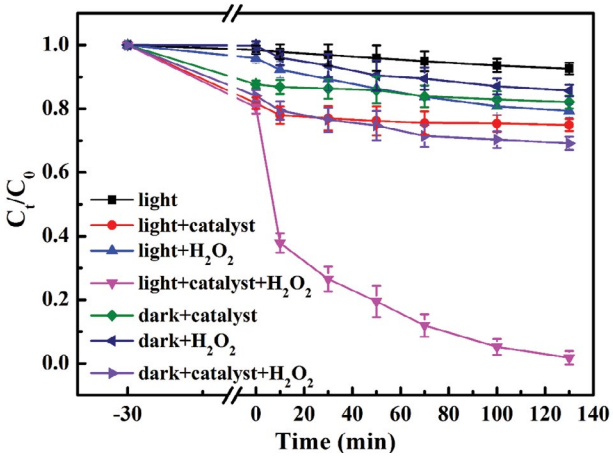

Fig. 7. Control experiments for the photocatalytic degradation of RhB.

increased, which was about 98.24%. Three experiments were carried out to explore the degradation efficiency of RhB under dark conditions. And all parameters were consistent. It could be seen that the catalyst had a certain adsorption capacity for RhB. When only adding catalysts the degradation efficiency of RhB within 150 min reached

about 20%. On the contrary, when only adding H_2O_2, it had a very low degradation efficiency of RhB, which was only about 9.52%. Meanwhile, the degradation efficiency of RhB was 30.84% in the presence of both catalyst and H_2O_2. By comparing the results of the comparative experiments, it could be seen that the catalyst added under the dark had a certain adsorption capacity to the RhB, but the adsorption capacity was weak. Only the catalyst or H_2O_2 was added under the light, the degradation efficiency of the RhB was not significantly improved. But when the catalyst and H_2O_2 were added to the RhB solution, the degradation efficiency of the RhB was greatly improved. These results showed that EDTMPA-Cu-LDH could be used as an effective catalyst for the heterogeneous oxidation of RhB.

3.2.2. Effect of pH on RhB degradation

The degradation efficiency and first-order-kinetic curves of the photocatalytic degradation of RhB under different pH are shown in Figs. 8a and b, respectively. It could be seen that, under weakly acidic conditions, the degradation efficiency of RhB was higher. The degradation efficiency was found to be higher at pH 5, which was 83.8%. And the rate constant for RhB degradation of under optimum pH was 0.0108 min^{-1}. It might be explained that the optimum pH could respond to H_2O_2 to produce •OH radicals to degrade the RhB dye molecules. But, under weakly acidic conditions, the change of pH had little impact on the degradation efficiency. Conversely, the degradation efficiency of RhB was low under alkaline conditions. This might be due to the decrease in the catalyst's adsorption capacity to the dye as the concentration of competitive hydroxyl ions (OH^-) increased. It could be also observed that, under weakly acidic conditions, the catalyst showed strong adsorption to RhB in the first 30 min. The larger the adsorption amount, the better the degradation effect. And the Cu ions in the catalyst would be eluted in a small amount to form a homogeneous reaction. The homogeneous reaction efficiency would generally be greater than the heterogeneous reaction, so the degradation efficiency would be increased. Since 5.85 was the natural pH of the RhB solution, therefore, further experiments were conducted without adjusting the pH.

3.2.3. Effect of initial concentration on RhB degradation

The effect of initial dye concentration on the degradation efficiency is depicted in Fig. 9a and first order-kinetic curves of the photocatalytic degradation of RhB under different dye concentration is shown in Fig. 9b. It could be observed that the degradation efficiency decreased with the increase of the concentration of the RhB solution. The maximum degradation efficiency was 97.1%. And the rate constant for RhB degradation under optimum dye concentration was 0.0248 min^{-1}. The reason for the observed changes could be that more and more dye molecules were adsorbed on the surface of the catalyst and occupying the active sites with the dye concentration increased. A large amount of adsorbed dye molecules could lead to a decrease in hydroxyl radicals and superoxide radicals generated on the catalyst during photocatalysis and be the lack of direct contact among and holes, hydroxyl radicals or superoxide radicals. Moreover, high dye concentration was likely to act as an inner filter which shunts the photons away from the catalyst surface. The adsorbed dye molecules blocked the active surface sites on the catalyst, thus reducing degradation efficiency.

3.2.4. Effect of H_2O_2 concentration on RhB degradation

The concentration of H_2O_2 was essential to the degradation of RhB dyes during photocatalysis. The degradation efficiency and first-order-kinetic curves of the photocatalytic degradation of RhB under different H_2O_2 concentrations are shown in Figs. 10a and b, respectively. The results indicated that the degradation efficiency increased with H_2O_2 concentration increased. When the concentration of H_2O_2 was 9 mmol L^{-1}, the degradation efficiency reached 94.3%. And the rate constant for RhB degradation under optimum H_2O_2 concentration was 0.01934 min^{-1}. This result was likely that hydrogen peroxide decomposed on the surface of the catalyst to produce more •OH with the increase of H_2O_2 concentration, which increased the degradation efficiency of RhB. However, the degradation efficiency increased negligibly when the H_2O_2 concentration increased from 7 to 9 mmol L^{-1} due to the generation of hydroperoxyl radicals ($HO_2^•$) [Eq. (5)], which could scavenge •OH [Eq. (6)]. Recombination of hydroxyl radicals at higher H_2O_2

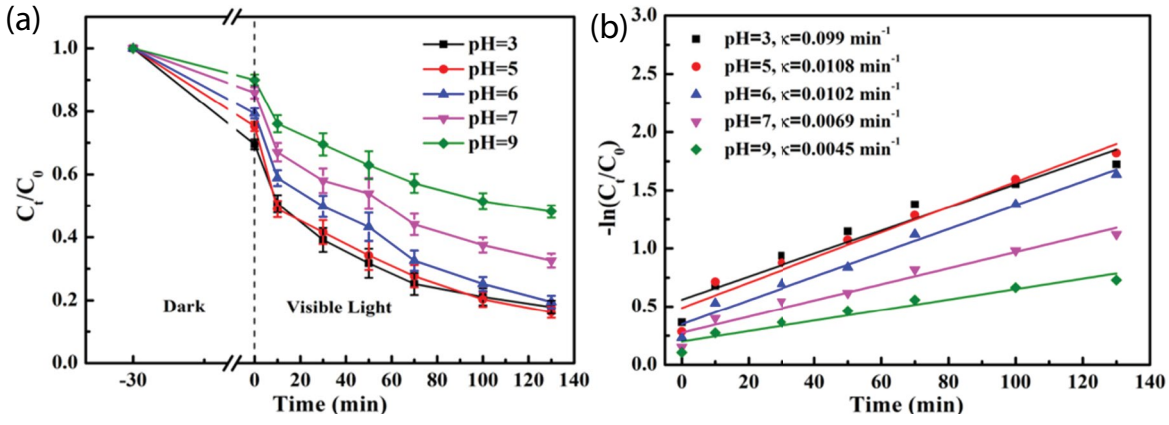

Fig. 8. The influence of pH on photodegradation of RhB (a), first-order-kinetic curves of the photocatalytic degradation of RhB under different pH (b).

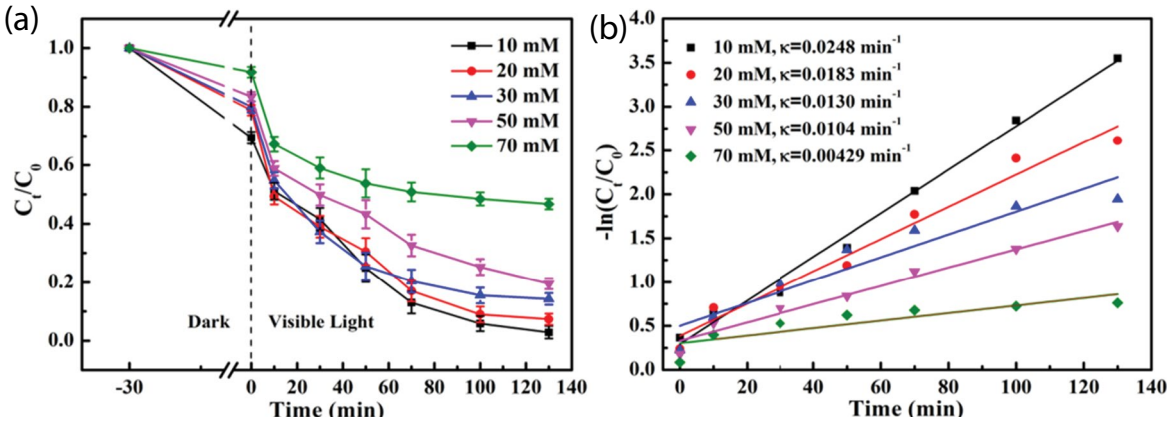

Fig. 9. The influence of initial dye concentration on photodegradation of RhB (a), first order-kinetic curves of the photocatalytic degradation of RhB under different dye concentration (b).

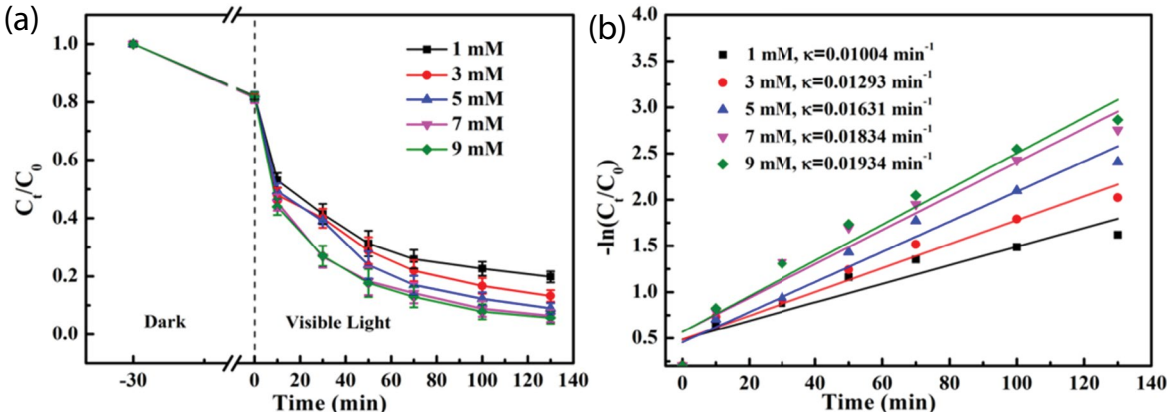

Fig. 10. The influence of H_2O_2 concentration on photodegradation of RhB (a), first-order-kinetic curves of the photocatalytic degradation of RhB under different H_2O_2 concentration (b).

concentrations also retarded dye removal efficiency [Eq. (7)]. The reaction could be expressed by the following equations:

$$^{\bullet}OH + H_2O_2 \rightarrow HO_2^{\bullet} + H_2O \quad (5)$$

$$HO_2^{\bullet} + {}^{\bullet}OH \rightarrow H_2O + O_2 \quad (6)$$

$$^{\bullet}OH + {}^{\bullet}OH \rightarrow H_2O_2 \quad (7)$$

To achieve a high degradation efficiency and prevent the occurrence of scavengers, the optimal H_2O_2 concentration was 7 mmol L^{-1}.

3.2.5. Effect of catalyst dosage on RhB degradation

The degradation efficiency and first-order-kinetic curves of the photocatalytic degradation of RhB under different catalyst dosage are shown in Figs. 11a and b, respectively. When the dosage of the catalyst was increased from 0.1 to 0.3 g L^{-1}, the degradation efficiency increased significantly. And the optimal degradation efficiency was 98.2%. And the rate constant for RhB degradation under optimum catalyst dosage was 0.02641 min^{-1}. The reason could be that the increased RhB degradation efficiency with increasing catalyst dosage indicated the increased the active sites on the surface of the catalyst and the more $^{\bullet}OH$ production. However, when the dosage of the catalyst exceeded 0.3 g L^{-1}, the degradation efficiency decreased obviously. The decrease in degradation efficiency was mainly due to the increased scavenging response at higher catalyst dosage. And more catalyst amount led to unfavorable light scattering and reduced light penetration into the solution. Therefore, the catalyst loading of 0.3 g L^{-1} could be considered as the optimum for RhB degradation.

3.3. Analysis of the mechanism of photocatalytic degradation of RhB

3.3.1. Detection of active species in EDTMPA-Cu-LDH heterophase photo-Fenton catalytic degradation of RhB

The detection of active species in the degradation mechanism of RhB was mainly explored by means of the scavenger experimental method. The degradation efficiency of RhB under different active species is shown in Fig. 12. Under the conditions of 0.3 g L^{-1} catalyst, 10 mmol L^{-1} RhB

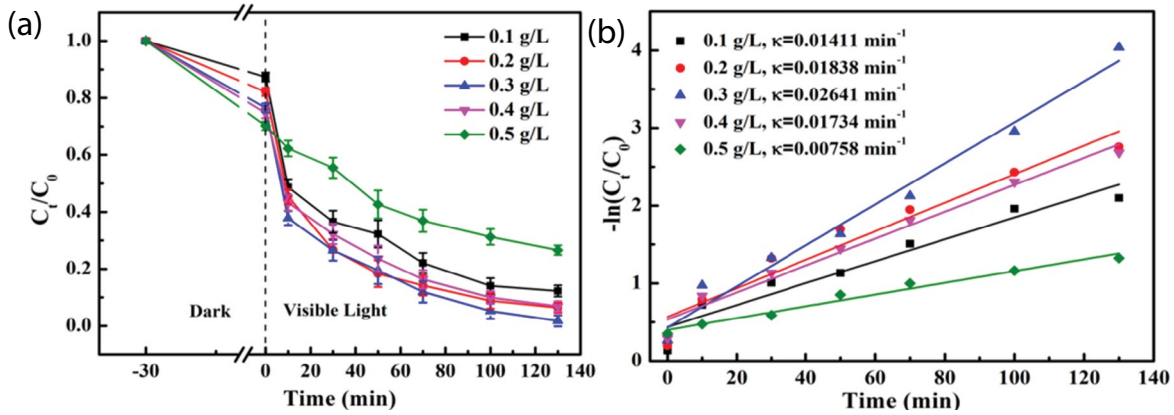

Fig. 11. The influence of catalyst dosage on photodegradation of RhB (a), first-order-kinetic curves of the photocatalytic degradation of RhB under different catalyst dosage (b).

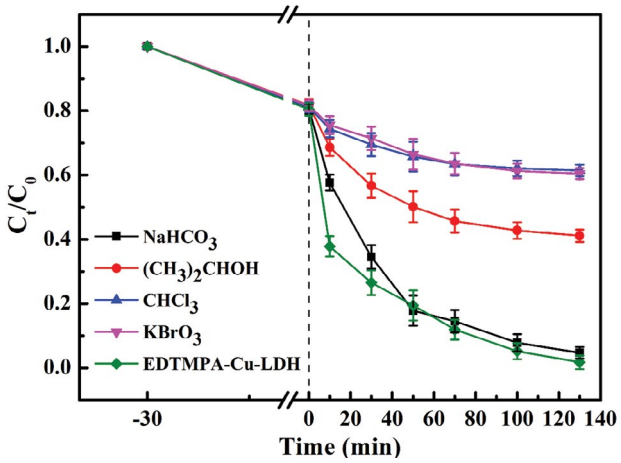

Fig. 12. The influence of different active species on photodegradation of RhB.

and 7 mmol L^{-1} H_2O_2, a sufficient amount of different active species of capture agent was added to the reaction solution. Generally speaking, sodium bicarbonate ($NaHCO_3$), IPA (C_3H_8O), chloroform ($CHCl_3$) and potassium bromate ($KBrO_3$) were used as scavenging reagents for trapping h^+, $^{\bullet}OH$ radicals, $^{\bullet}O_2^-$ radicals and e^-, respectively. When $NaHCO_3$ was added as hole trapping agent, the degradation efficiency of RhB decreased by only 2.95%, which indicated that h^+ effect was weak during the catalytic degradation process, but other active free radicals were at work. When a certain amount of IPA was added to the system, the degradation efficiency of RhB was significantly inhibited, from 98.24% to 39.36%, indicating $^{\bullet}OH$ was important role in RhB degradation. When a certain amount of $CHCl_3$ was added to the system, the degradation efficiency of RhB was strongly inhibited and the inhibition rate could reach 59.69%, which played a leading role in RhB degradation. When a certain amount of $KBrO_3$ was added to the reaction system, the degradation efficiency of RhB dropped slightly and the inhibition rate reached 58.71%. Therefore, the major reactive species accountable for the RhB degradation comprises $^{\bullet}OH$, $^{\bullet}O_2^-$, and e^- by using the EDTMPA-Cu-LDH catalyst.

3.3.2. Reaction mechanism of photocatalysis

The entire degradation reaction is likely to take place in a series of sequential reactions [Eqs. (8)–(13)] in the presence of visible light. The electrons are excited from the valence band (VB) to the conduction band (CB), leaving electron holes (h^+) in the valence band. Excitation is initiated by absorbing photons having energy equal to or greater than the band gap energy of the semiconductor material. Therefore, EDTMPA-Cu-LDH generates e^-–h^+ pairs [Eq. (8)] under visible light. The reason of superoxide radicals ($^{\bullet}O_2^-$) formation may be the reaction of electrons with oxygen adsorbed on the surface of the catalyst [Eq. (9)], which also has a strong oxidation ability, as shown in Fig. 13. H_2O_2, as an electron acceptor, is added to the photocatalytic system to suppress the recombination of electron-hole pair and generate more $^{\bullet}OH$ radicals [Eq. (10)]. The hydroxyl radicals ($^{\bullet}OH$) and superoxide radicals ($^{\bullet}O_2^-$) will degrade RhB into H_2O and CO_2 [Eq. (11)].

$$EDTMPA - Cu - LDH + hv \rightarrow h^+ + e^- \quad (8)$$

$$O_2 + e^- \rightarrow {}^{\bullet}O_2^- \quad (9)$$

$$H_2O_2 + {}^{\bullet}O_2^- \rightarrow {}^{\bullet}OH + OH^- \quad (10)$$

$$^{\bullet}O_2^- + {}^{\bullet}OH + RhB \rightarrow H_2O + CO_2 \quad (11)$$

3.4. Cyclic utilization and stability of EDTMPA-Cu-LDH

Recycling experiments were performed to evaluate the reusability of the EDTMPA-Cu-LDH catalyst for the degradation of RhB. The degradation efficiency of RhB under each circle is shown in Fig. 14. The initial concentration of RhB was 10 mmol L^{-1}. The concentration of H_2O_2 was 7 mmol L^{-1} and the catalyst dosage was 0.3 g L^{-1}. The reaction time for each cycle was 2 h. The used catalyst was collected from the solution by centrifugation after each reaction, then washed three times with ultrapure water, and dried at 50°C. The degradation efficiency for the first cycle was 98.7%.

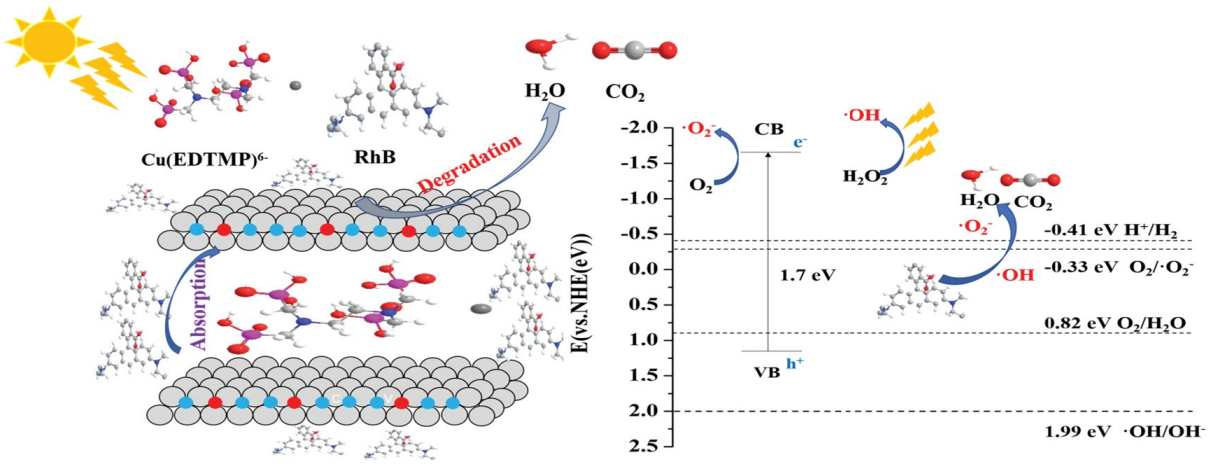

Fig. 13. A schematic illustration of the energy position and RhB degradation.

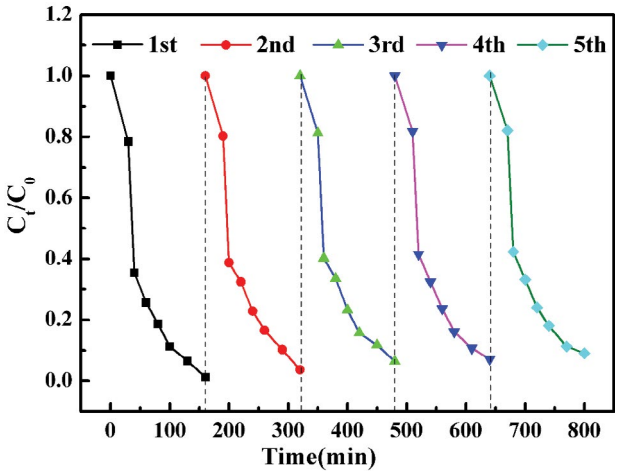

Fig. 14. The reuse time of RhB photodegradation efficiency.

Although the degradation efficiency was somewhat reduced in each cycle, the degradation efficiency was still 91% after five cycles. It indicated that the EDTMPA-Cu-LDH material as a heterogeneous Fenton catalyst possessed reusability and high stability.

4. Conclusions

In summary, heterogeneous catalyst EDTMPA-Cu-LDH was synthesized by co-precipitation method and showed high visible-light photocatalytic properties for degradation of RhB. The catalyst maintained cycling stability after five circles. The degradation kinetics followed first order model for the test dye. The photocatalysis proceeded through electron-hole hopping and by dye-sensitized mechanistic pathways. The optimum conditions for RhB degradation were found to be natural initial pH 5.85, 10 mmol L^{-1} of RhB concentration, 7 mmol L^{-1} of H_2O_2 concentration and 0.3 g L^{-1} of catalyst dosage. Under above condition, the maximun degradation efficiency was 98.2%. Based on the reactive species trapping experiments, $^{\bullet}OH$, $^{\bullet}O_2^-$, and e^- were considered to be the main active species for EDTMPA-Cu-LDH toward the degradation of RhB. From the results of this work, EDTMPA-Cu-LDH could be used as an effective and recyclable catalyst for large-scale wastewater treatment.

Acknowledgement

This work was supported by the Major Science and Technology Special Fund of Hubei Province, China (2018ACA154) and Science Research Fund of Wuhan Institute of Technology (K201516 and K201943).

References

[1] S. Rasalingam, C.-M. Wu, R.T. Koodali, Modulation of pore sizes of titanium dioxide photocatalysts by a facile template free hydrothermal synthesis method: implications for photocatalytic degradation of Rhodamine B, ACS Appl. Mater. Interfaces, 7 (2015) 4368–4380.

[2] J.H. Ma, W.J. Song, C.C. Chen, W.H. Ma, J.C. Zhao, Y.L. Tang, Fenton degradation of organic compounds promoted by dyes under visible irradiation, Environ. Sci. Technol., 39 (2005) 5810–5815.

[3] H. Lachheb, E. Puzenat, A. Houas, M. Ksibi, E. Elaloui, C. Guillard, J.M. Herrmann, Photocatalytic degradation of various types of dyes (Alizarin S, Crocein Orange G, Methyl Red, Congo Red, Methylene Blue) in water by UV-irradiated titania, Appl. Catal., B, 39 (2002) 75–90.

[4] Q.G. Lu, W. Gao, J.J. Du, L. Zhou, Y.H. Lian, Discovery of environmental Rhodamine B contamination in paprika during the vegetation process, J. Agric. Food Chem., 60 (2012) 4773–4778.

[5] X.Y. Sun, B. Liu, Y. Zhang, Rhodamine B aggregation in self-assembled multilayers induced by polyelectrolyte and interfacial fluorescence recognition for DNA, Talanta, 85 (2011) 1187–1192.

[6] J. Guo, S.J. Yuan, W. Jiang, H.R. Yue, Z. Cui, B. Liang, Adsorption and photocatalytic degradation behaviors of rhodamine dyes on surface-fluorinated TiO_2 under visible irradiation, RSC Adv., 6 (2016) 4090–4100.

[7] L. Zhang, C.-G. Niu, G.-X. Xie, X.-J. Wen, X.-G. Zhang, G.-M. Zeng, Controlled growth of BiOCl with large {010} facets for dye self-photosensitization photocatalytic fuel cells application, ACS Sustainable Chem. Eng., 5 (2017) 4619–4629.

[8] M. Cheng, G.M. Zeng, D.L. Huang, C. Lai, P. Xu, C. Zhang, Y. Liu, Hydroxyl radicals based advanced oxidation processes (AOPs) for remediation of soils contaminated with organic compounds: a review, Chem. Eng. J., 284 (2016) 582–598.

[9] M.M. Abdel daiem, J. Rivera-Utrilla, R. Ocampo-Pérez, J.D. Méndez-Díaz, M. Sánchez-Polo, Environmental impact of phthalic acid esters and their removal from water and sediments by different technologies — a review, J. Environ. Manage., 109 (2012) 164–178.
[10] Y.-S. Ma, C.-F. Sung, J.-G. Lin, Degradation of carbofuran in aqueous solution by ultrasound and Fenton processes: effect of system parameters and kinetic study, J. Hazard. Mater., 178 (2010) 320–325.
[11] H.B. Ammar, M.B. Brahim, R. Abdelhédi, Y. Samet, Enhanced degradation of metronidazole by sunlight via photo-Fenton process under gradual addition of hydrogen peroxide, J. Mol. Catal. A: Chem., 420 (2016) 222–227.
[12] B. Jiang, X.L. Wang, Y.K. Liu, Z.H. Wang, J.T. Zheng, M.B. Wu, The roles of polycarboxylates in Cr(VI)/sulfite reaction system: Involvement of reactive oxygen species and intramolecular electron transfer, J. Hazard. Mater., 304 (2016) 457–466.
[13] A.O. Ibhadon, P. Fitzpatrick, Heterogeneous photocatalysis: recent advances and applications, Catalysts, 3 (2013) 189–218.
[14] B. Palanivel, S.D. Mudisoodum perumal, T. Maiyalagan, V. Jayarman, C. Ayyappan, M. Alagiri, Rational design of $ZnFe_2O_4$/g-C_3N_4 nanocomposite for enhanced photo-Fenton reaction and supercapacitor performance, Appl. Surf. Sci., 498 (2019) 143807.
[15] T. Xian, L.J. Di, X.F. Sun, H.Q. Li, Y.J. Zhou, H. Yang, Photo-Fenton degradation of AO7 and photocatalytic reduction of Cr(VI) over CQD-decorated $BiFeO_3$ nanoparticles under visible and NIR light irradiation, Nanoscale Res. Lett., 14 (2019) 1–14.
[16] L. Lyu, L.L. Zhang, C. Hu, Enhanced Fenton-like degradation of pharmaceuticals over framework copper species in copper-doped mesoporous silica microspheres, Chem. Eng. J., 274 (2015) 298–306.
[17] L. Lyu, G.F. Yu, L.L. Zhang, C. Hu, Y. Sun, 4-Phenoxyphenol-functionalized reduced graphene oxide nanosheets: a metal-free Fenton-like catalyst for pollutant destruction, Environ. Sci. Technol., 52 (2017) 747–756.
[18] V. Singh, P. Bansal, Fabrication and characterization of needle shaped CuO nanoparticles and their application as photocatalyst for degradation of organic pollutants, Mater. Lett., 261 (2020) 126929
[19] S. Kayalvizhi, A. Sengottaiyan, T. Selvankumar, B. Senthilkumar, C. Sudhakar, K. Selvam, Eco-friendly cost-effective approach for synthesis of copper oxide nanoparticles for enhanced photocatalytic performance, Optik, 202 (2020) 163507.
[20] B.F. Sun, H.L. Li, X.Y. Li, X.W. Liu, C.H. Zhang, H.Y. Xu, X.S. Zhao, Degradation of organic dyes over Fenton-like Cu_2O–Cu/C catalysts, Ind. Eng. Chem. Res., 57 (2018) 14011–14021.
[21] K.A. Tarasov, D. O'Hare, V.P. Isupov, Solid-state chelation of metal ions by ethylenediaminetetraacetate intercalated in a layered double hydroxide, Inorg. Chem., 42 (2003) 1919–1927.
[22] Y.D. Zou, X.X. Wang, Y.J. Ai, Y.H. Liu, J.X. Li, Y.F. Li, X.K. Wang, Coagulation behavior of graphene oxide on nanocrystallined Mg/Al layered double hydroxides: batch experimental and theoretical calculation study, Environ. Sci. Technol., 50 (2016) 3658–3667.
[23] Z.H. Li, M.F. Shao, L. Zhou, R.K. Zhang, C. Zhang, M. Wei, D.G. Evans, X. Duan, Directed growth of metal-organic frameworks and their derived carbon-based network for efficient electrocatalytic oxygen reduction, Adv. Mater., 28 (2016) 2337–2344.
[24] J. Li, Q.H. Fan, Y.J. Wu, X.X. Wang, C.L. Chen, Z.Y. Tang, X.K. Wang, Magnetic polydopamine decorated with Mg–Al LDH nanoflakes as a novel bio-based adsorbent for simultaneous removal of potentially toxic metals and anionic dyes, J. Mater. Chem. A, 4 (2016) 1737–1746.
[25] M.S.S. Dorraji, M.H. Rasoulifard, H. Daneshvar, A. Vafa, A.R. Amani-Ghadim, ZnS/ZnNiAl-LDH/GO nanocomposite as a visible-light photocatalyst: preparation, characterization and modeling, J. Mater. Sci. - Mater. Electron., 30 (2019) 12152–12162.
[26] S. Nayak, G. Swain, K. Parida, Enhanced photocatalytic activities of RhB degradation and H_2 evolution from in situ formation of the electrostatic heterostructure MoS_2/NiFe LDH nanocomposite through the Z-scheme mechanism via *p*–*n* heterojunctions, ACS Appl. Mater. Interfaces, 11 (2019) 20923–20942.
[27] A. Mantilla, G. Jácome-Acatitla, G. Morales-Mendoza, F. Tzompantzi, R. Gómez, Photoassisted degradation of 4-chlorophenol and *p*-cresol using MgAl hydrotalcites, Ind. Eng. Chem. Res., 50 (2011) 2762–2767.
[28] Y.H. Chuang, Y.M. Tzou, M.K. Wang, C.H. Liu, P.N. Chiang, Removal of 2-chlorophenol from aqueous solution by Mg/Al layered double hydroxide (LDH) and modified LDH, Ind. Eng. Chem. Res., 47 (2008) 3813–3819.
[29] L.P. Fang, W.T. Li, H.M. Chen, F. Xiao, L.Z. Huang, P.E. Holm, H.C.B. Hansen, D.S. Wang, Synergistic effect of humic and fulvic acids on Ni removal by the calcined Mg/Al layered double hydroxide, RSC Adv., 5 (2015) 18866–18874.
[30] N. Stojilovic, D.E. Isaacs, Inquiry-based experiment with powder XRD and FeS_2 crystal: "discovering" the (400) peak, J. Chem. Educ., 96 (2019) 1449–1452.
[31] Y. Zhang, J.Q. Yang, F.Y. Fan, B.J. Qing, C.L. Zhu, Y.F. Shi, J. F, X.C. Deng, Effect of divalent metals on the UV-shielding properties of M^{II}/MgAl layered double hydroxides, ACS Omega, 4 (2019) 10151–10159.
[32] J. Li, H.Z. Cui, X.J. Song, G.S. Zhang, X.Z. Wang, Q. Song, N. Wei, J. Tian, Adsorption and intercalation of organic pollutants and heavy metal ions into MgAl-LDH s nanosheets with high capacity, RSC Adv., 6 (2016) 92402–92410.
[33] C.S. Lu, M.J. Wang, Z.L. Feng, Y.N. Qi, F. Feng, L. Ma, Q.F. Zhang, X.N. Li, A phosphorus–carbon framework over activated carbon supported palladium nanoparticles for the chemoselective hydrogenation of *para*-chloronitrobenzene, Catal. Sci. Technol., 7 (2017) 1581–1589.
[34] G. Fonder, I. Minet, C. Volcke, S. Devillers, J. Delhalle, Z. Mekhalif, Anchoring of alkylphosphonic derivatives molecules on copper oxide surfaces, Appl. Surf. Sci., 257 (2011) 6300–6307.
[35] P.J. Hotchkiss, M. Malicki, A.J. Giordano, N.R. Armstrong, S.R. Marder, Characterization of phosphonic acid binding to zinc oxide, J. Mater. Chem., 21 (2011) 3107–3112.
[36] H. Chai, Y.J. Lin, D.G. Evans, D.Q. Li, Synthesis and UV absorption properties of 2-naphthylamine-1,5-disulfonic acid intercalated Zn–Al layered double hydroxides, Ind. Eng. Chem. Res., 47 (2008) 2855–2860.
[37] H.T. Handal, A. Hassan, R. Leeson, S.M. Eloui, M. Fitzpatrick, V. Thangadurai, Profound understanding of effect of transition metal dopant, sintering temperature, and pO_2 on the electrical and optical properties of proton conducting $BaCe_{0.9}Sm_{0.1}O_{3-\delta}$, Inorg. Chem., 55 (2015) 729–744.
[38] C.F. Zhang, L.G. Qiu, F. Ke, Y.J. Zhu, Y.P. Yuan, G.S. Xu, X. Jiang, A novel magnetic recyclable photocatalyst based on a core–shell metal–organic framework Fe_3O_4@MIL-100(Fe) for the decolorization of methylene blue dye, J. Mater. Chem. A, 1 (2013) 14329–14334.
[39] T. Gao, S. Hou, K. Huynh, F. Wang, N. Eidson, X.L. Fan, F.D. Han, C. Luo, M.L. Mao, X.G. Li, C.S. Wang, Existence of solid electrolyte interphase in Mg batteries: Mg/S chemistry as an example, ACS Appl. Mater. Interfaces, 10 (2018) 14767–14776.
[40] J.G. Connell, B. Genorio, P.P. Lopes, D. Strmcnik, V.R. Stamenkovic, N.M. Markovic, Tuning the reversibility of Mg anodes via controlled surface passivation by H_2O/Cl^- in organic electrolytes, Chem. Mater., 28 (2016) 8268–8277.
[41] D.Q. Gao, J. Zhang, G.J. Yang, J.L. Zhang, Z.H. Shi, J. Qi, Z.H. Zhang, D.S. Xue, Ferromagnetism in ZnO nanoparticles induced by doping of a nonmagnetic element: Al, J. Phys. Chem. C, 114 (2010) 13477–13481.
[42] B. Zhang, R.T. Hu, D.J. Sun, T. Wu, Y.J. Li, Fabrication of magnetite-graphene oxide/MgAl-layered double hydroxide composites for efficient removal of emulsified oils from various oil-in-water emulsions, J. Chem. Eng. Data, 63 (2018) 4689–4702.
[43] A.Y. Yin, X.Y. Guo, W.-L. Dai, K.N. Fan, Effect of Si/Al ratio of mesoporous support on the structure evolution and catalytic performance of the Cu/Al-HMS catalyst, J. Phys. Chem. C, 114 (2010) 8523–8532.
[44] W. Zhang, X.H. He, G. Ye, R. Yi, J. Chen, Americium(III) capture using phosphonic acid-functionalized silicas with

different mesoporous morphologies: adsorption behavior study and mechanism investigation by EXAFS/XPS, Environ. Sci. Technol., 48 (2014) 6874–6881.
[45] X.D. Zhao, T. Wang, G.H. Du, M.Q. Zheng, S.X. Liu, Z.Y. Zhang, Y.Z. Zhang, X.L. Gao, Z.Q. Gao, Effective removal of humic acid from aqueous solution in an Al-based metal–organic framework, J. Chem. Eng. Data, 64 (2019) 3624–3631.
[46] A. Mocellin, A.H. de Abreu Gomes, O.C. Araújo, A.N. de Brito, O. Björneholm, Surface propensity of atmospherically relevant amino acids studied by XPS, J. Phys. Chem. B, 121 (2017) 4220–4225.
[47] Y.J. Kim, C.R. Park, Analysis of problematic complexing behavior of ferric chloride with *N,N*-dimethylformamide using combined techniques of FT-IR, XPS, and TGA/DTG, Inorg. Chem., 41 (2002) 6211–6216.